

# Experimental Surface Strain Mapping of Porcine Peripapillary Sclera Due to Elevations of Intraocular Pressure

**Michaël J. A. Girard**

Department of Biomedical Engineering,  
Tulane University,  
6823 St. Charles Avenue,  
New Orleans, LA 70118;  
Ocular Biomechanics Laboratory,  
Devers Eye Institute,  
Legacy Health System,  
1225 NE 2nd Avenue,  
Portland, OR 97232  
e-mail: mgirard@deverseye.org,  
michael.girard@mac.com

**J. Crawford Downs**

Ocular Biomechanics Laboratory,  
Devers Eye Institute,  
Legacy Health System,  
1225 NE 2nd Avenue,  
Portland, OR 97232

**Claude F. Burgoyne**

Optic Nerve Head Research Laboratory,  
Devers Eye Institute,  
Legacy Health System,  
1225 NE 2nd Avenue,  
Portland, OR 97232;

**J.-K. Francis Suh**

Moksan BioEng LLC,  
605 Middle Street Unit #25,  
Braintree, MA 02184

*To experimentally characterize 2D surface mapping of the deformation pattern of porcine peripapillary sclera following acute elevations of intraocular pressure (IOP) from 5 mm Hg to 45 mm Hg. Four porcine eyes were obtained within 48 h postmortem and dissected to the sclera. After the anterior chamber was removed, each posterior scleral shell was individually mounted at the equator on a custom-built pressurization device, which internally pressurized the scleral samples with isotonic saline at 22°C. Black polystyrene microspheres (10 μm in diameter) were randomly scattered and attached to the scleral surface. IOP was incrementally increased from 5 mm Hg to 45 mm Hg ( $\pm 0.15$  mm Hg), and the surface deformation of the peripapillary sclera immediately adjacent to the dural insertion was optically tracked at a resolution of 2 μm/pixel one quadrant at a time, for each of four quadrants (superior, nasal, inferior, and temporal). The 2D displacement data of the microsphere markers were extracted using the optical flow equation, smoothed by weighting function interpolation, and converted to the corresponding Lagrangian finite surface strain. In all four quadrants of each eye, the principal strain was highest and primarily circumferential immediately adjacent to the scleral canal. Average maximum Lagrangian strain across all quadrants for all eyes was  $0.013 \pm 0.005$  from 5 mm Hg to 10 mm Hg,  $0.014 \pm 0.004$  from 10 mm Hg to 30 mm Hg and  $0.004 \pm 0.001$  from 30 mm Hg to 45 mm Hg, demonstrating the nonlinearity in the IOP-strain relationship. For each scleral shell, the observed surface strain mapping implied that the scleral stiffness was relatively low between 5 mm Hg and 10 mm Hg, but dramatically increased for each IOP elevation increment beyond 10 mm Hg. Peripapillary deformation following an acute IOP elevation may be governed by the underlying scleral collagen microstructure and is likely in the high-stiffness region of the scleral stress-strain curve when IOP is above 10 mm Hg. [DOI: 10.1115/1.2948416]*

*Keywords:* ocular biomechanics, sclera, intraocular pressure

## Introduction

Glaucomatous optic neuropathy is one of the three leading causes of blindness in the U.S. [1]. We hypothesize that the mechanical properties of peripapillary and posterior sclera are altered during the disease and play a significant role in the development and progression of glaucomatous damage to the neural and connective tissues within the optic nerve head (ONH) [2].

In order to evaluate the effect of elevated intraocular pressure (IOP) on the connective tissues of the posterior pole and ONH, finite element models of the posterior pole of the eye are being constructed in our laboratory [2]. The ultimate goal of our work is to fully characterize the mechanical behavior of each tissue within and around the ONH, and to investigate how the mechanical environment in the ONH influences the onset and progression of glaucoma. To build these models, accurate characterization of the material properties of the load-bearing tissues is necessary. Preliminary work has been done on the material properties of monkey and rabbit peripapillary sclera using uniaxial tensile testing [3–5], and this study extends those methodologies to pressure testing techniques.

The sclera is the outer shell and principal load-bearing tissue of the eye, which consists primarily of avascular lamellae of collagen fibers [6]. 90% of the collagen fibers in the sclera are Type I, which provide mechanical integrity and tensile strength. The posterior sclera contains the scleral canal, which is spanned by a fenestrated connective tissue structure known as the lamina cribrosa. The retinal ganglion cell axons that transmit visual signals from the retina to the brain pass through these fenestrations. This region is known as the ONH and is the principal site of damage in glaucoma [2]. We believe that ONH biomechanics plays a significant role in the development and progression of glaucoma, and the mechanical properties of the peripapillary sclera determine the extent to which the scleral canal deforms in response to elevated IOP.

In our previous studies [3–5], experimental and mathematical models were used to determine the uniaxial mechanical properties of the sclera, and the tissue was assumed to be linearly viscoelastic and isotropic. While this was a good first step, the sclera is a complex structure with varying collagen fiber orientation [7–10], so its mechanical behavior under IOP-induced mechanical stress is likely to be anisotropic and nonlinear. Hence, uniaxial testing is likely to be insufficient to predict the mechanical behavior of the tissue *in vivo*, and a more physiological testing protocol is necessary to fully describe the 3D behavior of the sclera in response to IOP elevations.

This current report presents a method to experimentally characterize the surface deformation pattern of porcine peripapillary

Contributed by the Bioengineering Division of ASME for publication in the JOURNAL OF BIOMECHANICAL ENGINEERING. Manuscript received July 22, 2007; final manuscript received April 18, 2008; published online June 20, 2008. Review conducted by Andrew D McCulloch. Paper presented at the Association for Research in Vision and Ophthalmology, Annual Meeting, Fort Lauderdale, FL, May 2005.

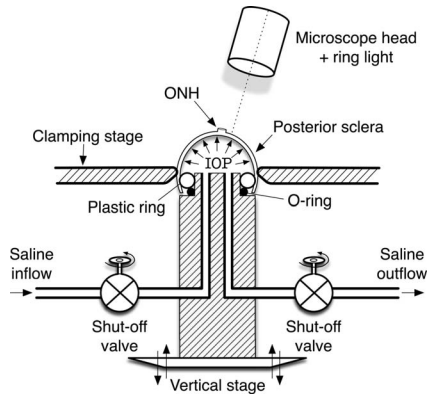


**Fig. 1** Schematic showing a cross section of the custom-built pressurization apparatus. The posterior scleral shell was first mounted onto the plastic ring, and then clamped at the equator by moving the vertical stage toward the clamping stage. The saline outflow was interrupted after saline filled the posterior shell cavity and IOP reached 5 mm Hg. The scleral surface was imaged as IOP was increased from 5 mm Hg to 45 mm Hg with an increment of 1 mm Hg.

sclera exposed to IOP ranging from 5 mm Hg to 45 mm Hg. The method described herein can be applied to thin soft tissues that are mechanically loaded with uni- and multi-axial testing protocols.

## Materials and Methods

**Experimental Setup and Testing Protocol.** Four porcine eyes were harvested from a slaughterhouse and stored in a phosphate buffered saline (PBS) solution at 4°C for 48 h until the experiments were conducted. A previous study [5] reported that donor eyes can be stored up to 72 h at 4°C in PBS without risking deterioration of the uniaxial mechanical behavior of the sclera.

At the time of experiments, the anterior chamber, vitreous, retina, and choroid of each eye were removed in order to isolate the posterior half of the sclera, which was then mounted and clamped at the equator on a custom-built pressurization apparatus (Fig. 1).

Pneumatic control of saline inflow and outflow was driven by a pressure regulator (Model 81, Fairchild, Winston-Salem, NC), which allowed each posterior scleral sample to be pressurized with a resolution of 0.15 mm Hg. Before the experiment, each pressurized scleral sample was quickly blotted with a gauze pad, and black dyed microspheres (10 μm diameter Polybead Polystyrene Microspheres, Polysciences, Inc, Warrington, PA), dissolved in a 70% ethanol solution, were randomly scattered onto the tissue surface. The microspheres were allowed to adhere to the scleral surface for 5 min while the ethanol dried and were used as surface markers for the optical tracking method described below. All tissue samples were then kept moist with drops of PBS applied throughout the entire experiment, which only minimally affected the optical tracking of the surface marker position.

Each scleral shell was subjected to IOP preconditioning, consisting of twenty IOP cycles from 5 mm Hg to a maximum of 15 mm Hg at a rate of 5 mm Hg/s, and then allowed to recover for 360 s.

An optical measurement system, consisting of a high-resolution microscope (SZX-12, Olympus, Center Valley, PA) and a high-resolution digital camera (MicroFire, Optronics, Goleta, CA), was employed to capture images of the markers at a resolution of 2 μm/pixel within a 4 × 4 mm<sup>2</sup> region of sclera. These images were acquired for each of the four quadrants of the peripapillary sclera around the ONH, in the following sequence: superior (S), nasal (N), inferior (I), and temporal (T) (Fig. 2(a)). Pixel resolution was calibrated using a slide mounted micrometer scale, and the sclera was illuminated using a fiber optic ring light to ensure

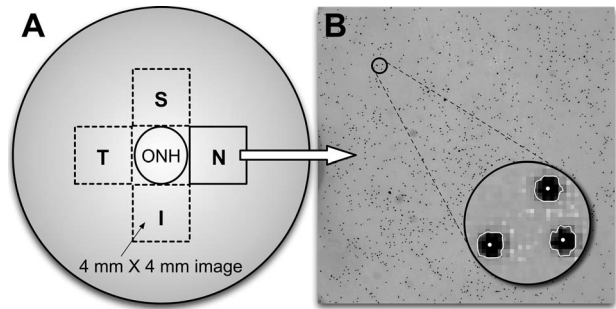


**Fig. 2** (a) Diagram of the posterior scleral shell of a left eye (OS) showing the position of the four fields of view within which 2D scleral deformation patterns were determined. Each field of view is 4 × 4 mm<sup>2</sup> with a single image resolution of 2 μm/pixel. (b) Image of a nasal quadrant with microsphere markers present on the surface of the shell and a magnified view of three microspheres showing their contours and centroids.

even illumination.

For each scleral shell, pressure was slowly increased by incremental steps of 1 mm Hg, from 5 mm Hg to 45 mm Hg, and images were generated for the inferior quadrant only. Each scleral shell was then depressurized from 45 mm Hg to 5 mm Hg until equilibrium was reached, and the process of image acquisition was repeated three times for the three other (temporal, nasal, and superior) quadrants. Each image was postprocessed with a sharpening filter to increase the contrast of the surface marker image, then a contour was defined for each marker, and its centroid was calculated (Fig. 2(b)).

Based on the set of images generated for each quadrant, the 2D displacement field was extracted using the optical flow equation as described below, which allowed accurate tracking of the markers for each 1 mm Hg elevation of IOP.

**Optical Flow Algorithm for Marker Tracking.** Manually tracking the movements of hundreds of markers in each image is a daunting and time-consuming process. This study, therefore, utilized RGB digital images of markers and an optical flow algorithm to automate the tracking of marker movements, from which the pixel displacement of each marker could be determined.

It was assumed that scleral illumination was uniform and the intensity of the markers did not change with motion from one image to the next. Considering the pixel intensity  $I_k$  of a RGB image, the previous assumption can be mathematically transcribed to

$$dI_k = 0, \quad k \in [1,3] \quad (1)$$

Here, the index  $k$  ranges from 1 to 3 corresponding to the three components of a RGB image (i.e., red, green, and blue). The pixel intensity  $I_k$  of the 2D image of the marker can be expressed as a function of space and time,  $I_k(x,y,t)$ , in which  $x$  and  $y$  represent the pixel coordinates. Taylor's first order approximation of Eq. (1) can be rewritten as

$$\frac{\partial I_k(x,y,t)}{\partial t} \cdot dt + \frac{\partial I_k(x,y,t)}{\partial x} \cdot dx + \frac{\partial I_k(x,y,t)}{\partial y} \cdot dy = 0, \quad k \in [1,3] \quad (2)$$

or

$$\frac{\partial I_k(x,y,t)}{\partial t} + \frac{\partial I_k(x,y,t)}{\partial x} \cdot v_x + \frac{\partial I_k(x,y,t)}{\partial y} \cdot v_y = 0, \quad k \in [1,3] \quad (3)$$

where  $v_x$  and  $v_y$  are defined as the pixel velocity components. Equation (3) is known as the color optical flow equation [11] and

can be applied to two 2D color pixel images taken at two consecutive time points.

A large body of work has been done to solve the optical flow equation using numerical approximations. Barron et al. [12] summarized and evaluated the most commonly used optical flow algorithms and their performance. For the present study, we chose to adopt the Lucas–Kanade algorithm [13,12], as described below because our preliminary comparative study found this reliable for RGB images [11].

If each image is captured at a physical equilibrium state, the time variable becomes secondary in Eq. (2). It is then reasonable to approximate Eq. (2) with  $dx=u_x$  and  $dy=u_y$ , where  $u_x$  and  $u_y$  are defined as the pixel displacements. In the Lucas–Kanade approximation [13,12], the displacement field can be assumed to be smooth over a region of interest,  $R$ , such that for each pixel, the adjacent pixels are subjected to the same displacement field. As a result, if  $R$  is a square patch of  $3 \times 3$  pixels with the pixel of interest in the center of that region, it requires a total of nine equations to be solved for each color channel (red, green, and blue) for the center pixel of  $R$ . This results in an overdetermined system of 27 equations with two unknowns to be solved for the center pixel, which can be rearranged in a matrix equation form:

$$\underbrace{\begin{pmatrix} \frac{\partial I_1(x_1, y_1)}{\partial x} & \frac{\partial I_1(x_1, y_1)}{\partial y} \\ \frac{\partial I_2(x_1, y_1)}{\partial x} & \frac{\partial I_2(x_1, y_1)}{\partial y} \\ \vdots & \vdots \\ \frac{\partial I_3(x_9, y_9)}{\partial x} & \frac{\partial I_3(x_9, y_9)}{\partial y} \end{pmatrix}}_{\mathbf{M}} \begin{pmatrix} u_x \\ u_y \end{pmatrix} = - \underbrace{\begin{pmatrix} \frac{\partial I_1(x_1, y_1)}{\partial t} \\ \frac{\partial I_2(x_1, y_1)}{\partial t} \\ \vdots \\ \frac{\partial I_3(x_9, y_9)}{\partial t} \end{pmatrix}}_{\mathbf{b}} dt \quad (4)$$

where  $(x_i, y_i)$  for  $i \in [1, 9]$  are the pixel coordinates of the region of interest  $R$ , and  $I_k$  for  $k \in [1, 3]$  are the corresponding RGB pixel intensities.

Using the least squares minimization method, Eq. (4) can be left multiplied by the matrix transpose of  $\mathbf{M}$ ,

$$\mathbf{M}^T \cdot \mathbf{M} \cdot \begin{pmatrix} u_x \\ u_y \end{pmatrix} = \mathbf{M}^T \cdot \mathbf{b} \quad (5)$$

For each pixel, therefore, the displacements can be simply expressed as

$$\begin{pmatrix} u_x \\ u_y \end{pmatrix} = (\mathbf{M}^T \cdot \mathbf{M})^{-1} \cdot \mathbf{M}^T \cdot \mathbf{b} \quad (6)$$

The solution of Eq. (6) was computed for each pixel and repeated over the entire pixel domain in the two consecutive images taken before and after each 1 mm Hg IOP increment. The partial derivatives  $\partial I_k / \partial x$ ,  $\partial I_k / \partial y$  in Eq. (4) were estimated using a seven-point rule, and the term  $(\partial I_k / \partial t) \cdot dt$ , with a two-point rule.

Using the aforementioned optical flow algorithm, Eqs. (3)–(6), the spatial coordinates  $X_C(i)$  and  $Y_C(i)$  of the centroid of each surface marker were processed to estimate its pixel displacement vector  $\{u_{Cx}(i), u_{Cy}(i)\}$  after the incremental IOP increase. Once the pixel displacement of a marker centroid was estimated by the aforementioned optical flow algorithm, a small circular area around the estimated centroid location  $\{X_C(i) + u_{Cx}(i), Y_C(i) + u_{Cy}(i)\}$  with a diameter of two pixels was searched to locate any marker centroid in the second image, as shown in Fig. 3. This newly located marker centroid was then registered as the true marker centroid after the deformation. This step was repeated for each particle in the image, for each 1 mm Hg pressure increment, and summed over an IOP elevation from 5 mm Hg to 45 mm Hg. Hence, the actual displacement vector was accurately determined

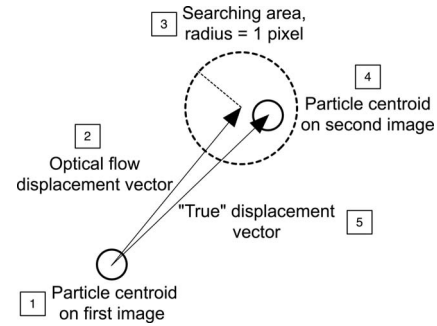


**Fig. 3** The optical flow displacement vector was used as an initial guess to derive the true displacement vector. The steps were as follows and were repeated for each 1 mm Hg IOP increase: (1) The coordinates of the particle centroids were determined on the first image. (2) The optical flow algorithm was executed to derive the predicted displacements. (3) For each particle, the optical flow displacement vector was added to the particle centroid coordinates, and a two pixel diameter search area was created. (4) The matching particle centroid on the second image was found in the search area. (5) For each particle, subtracted centroid coordinates yielded the true displacement vector.

for the IOP elevations from 5 mm Hg to 10 mm Hg, from 10 mm Hg to 30 mm Hg, and from 30 mm Hg to 45 mm Hg.

**Preliminary Validation of the Tracking Method Using a Rubber Balloon.** The experimental protocol and the optical flow algorithm method were validated using a half-spherical rubber balloon mounted and imaged as described previously, for incremental pressure increases from 70 mm Hg to 80 mm Hg. The images were acquired within a  $4 \times 4$  mm<sup>2</sup> region located midway between the equator and the pole of the balloon. The displacement field vector was generated for each 1 mm Hg pressure increment using the optical flow algorithm method. Since rubber is an isotropic, homogeneous elastic material, and the balloon wall is of relatively constant thickness, the resulting 2D displacement vector field as observed from the camera should be radial from the center of the image field.

**Determination of Lagrangian Strain Field.** After the displacement vector field was determined by the optical flow algorithm, the Lagrangian strain field on the scleral surface was calculated. To accomplish this, the  $4 \times 4$  mm<sup>2</sup> domain in each field image was first meshed with equal sized four-noded quadrilateral finite elements, and the nodal displacements were smoothed from the above displacement vector field using the thin plate smoothing spline method (MATLAB, The Mathworks, Natick, MA). For each quadrilateral element, a continuous displacement field function was then approximated by a bilinear interpolation function as

$$\begin{cases} u_x(x, y) = a_1 + a_2x + a_3y + a_4xy \\ u_y(x, y) = a_5 + a_6x + a_7y + a_8xy \end{cases} \quad (7)$$

in which the coefficients,  $a_i$ , could be determined from the nodal displacement values. The Lagrangian strain tensor  $\mathbf{E}$  was calculated at Gaussian points in each quadrilateral element as

$$\mathbf{E}(x, y) = \frac{1}{2} (\mathbf{F}^T(x, y) \cdot \mathbf{F}(x, y) - \mathbf{I}) \quad (8)$$

where  $\mathbf{F}$  is the deformation gradient tensor expressed as

Balloon experimental displacement field

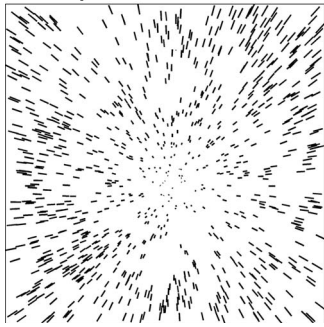


Fig. 4 Experimental displacement field for a 4×4 mm<sup>2</sup> location at the surface of a spherical rubber balloon. The microscope head was oriented perpendicular to the balloon surface and the displacement field was generated for a pressure ranging from 70 mm Hg to 80 mm Hg.

$$\mathbf{F}(x,y) = \begin{bmatrix} \frac{\partial u_x}{\partial x} + 1 & \frac{\partial u_x}{\partial y} \\ \frac{\partial u_y}{\partial x} & \frac{\partial u_y}{\partial y} + 1 \end{bmatrix} \quad (9)$$

The magnitudes and directions of the corresponding principal Lagrangian strain were also obtained by calculating the eigenvalues and eigenvectors of the Lagrangian strain tensor shown in Eq. (8), respectively. It should be noted that the posterior scleral geometry pressurized to 5 mm Hg was chosen as the reference configuration. Therefore, all Lagrangian strains mentioned in this study were computed from this reference configuration.

## Results

**Validation Results With Rubber Balloon.** The experimental displacement field obtained from a rubber balloon as a part of validation process of the optical flow method is shown in Fig. 4. The pattern of the displacement field was radial and was qualitatively very similar to that of an isotropic, homogeneous spherical pressure vessel. For the entire 4×4 mm<sup>2</sup> region, displacement components  $u$  and  $v$  were well fitted with two surface planes.

The Lagrangian strain tensor was calculated according to Eq. (8), and its maximum and minimum principal strains were found to be 0.90% and 0.79%, respectively. Although the maximum and minimum principal strains obtained for the rubber balloon were not exactly identical, they were close enough so that the rubber material could be assumed to be quasi-isotropic.

**Experimental Results With Porcine Specimen.** Figures 5 and 6 illustrate that the maximum principal strain was highest and primarily circumferential in trajectory in the peripapillary scleral region (immediately adjacent to the scleral canal). All four porcine eyes tested showed this specific pattern. However, the strain pattern was nonspecific in the peripheral scleral region further away from the scleral canal. Maximum increase of the principal Lagrangian strain for each IOP increase was averaged for all quadrants and for all specimens, and was found to be 0.013±0.005 for an IOP elevation from 5 mm Hg to 10 mm Hg ( $\Delta$ IOP=5 mm Hg), 0.014±0.004 for an IOP elevation from 10 mm Hg to 30 mm Hg ( $\Delta$ IOP=20 mm Hg), and 0.004±0.001 for an IOP elevation from 30 mm Hg to 45 mm Hg ( $\Delta$ IOP=15 mm Hg). This result shows that the additional strain per unit increase in IOP was significantly lower at higher IOPs, demonstrating a high degree of nonlinearity in the IOP-maximum principal strain relationship. For each posterior scleral shell, this surface strain mapping also

Principal Direction Associated with Maximum Principal Strain

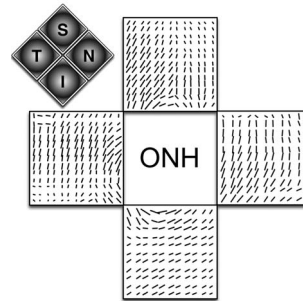


Fig. 5 Principal direction associated with maximum principal strain for a porcine scleral shell (OS) due to an IOP increase from 10 mm Hg to 30 mm Hg. All four porcine eyes that were tested showed the same specific patterns, for all four quadrants and for all IOP ranges (i.e., 5–10 mm Hg, 10–30 mm Hg, and 30–45 mm Hg).

implied that the scleral stiffness was relatively low for low IOPs (<10 mm Hg), but dramatically increased at higher IOPs (>10 mm Hg), as shown in Fig. 7.

## Discussion

In this report, a new experimental method was developed to measure the surface strain in thin materials. This methodology has wide applicability to uni- and multi-axial mechanical testing of

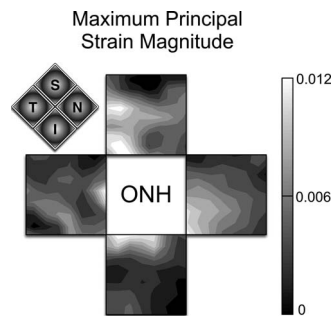


Fig. 6 Maximum principal strain magnitude for a porcine scleral shell (OS) due to an IOP increase from 10 mm Hg to 30 mm Hg. All four porcine eyes that were tested showed the same specific patterns, for all four quadrants and for all IOP ranges (i.e., 5–10 mm Hg, 10–30 mm Hg, and 30–45 mm Hg).

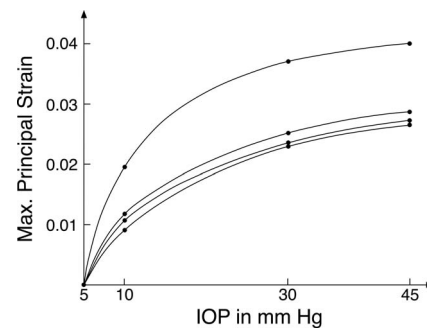


Fig. 7 Mean maximum increase of the maximum principal strain as a function of IOP for each of the four porcine eyes, showing the high degree of nonlinearity in the response. For each eye, means were calculated for all four quadrants pooled together. As IOP increases, porcine sclera becomes considerably stiffer.

thin soft tissues. In this study, we performed mechanical testing of porcine peripapillary sclera using a pressurization apparatus to induce elevations of IOP from 5 mm Hg to 45 mm Hg. For the four porcine scleral shells that were tested, the maximum principal strain magnitude was a nonlinear function of the applied IOP. The maximum principal strain was highest in magnitude and was circumferential in trajectory in the peripapillary region immediately adjacent to the scleral canal.

The nonlinear IOP-sclera strain relationship may be due to the collagen fibers in the sclera. It is well known that, under tension, collagen fibers exhibit a characteristic nonlinear stress-strain curve consisting of the initial “toe” region of low elastic modulus and the subsequent “linear” region of higher elastic modulus [14]. Our data would suggest that collagen fibers in the porcine sclera could have been in the linear elastic region when IOP is beyond 30 mm Hg. Additional experiments that consider a broader IOP range (e.g., 5–100 mm Hg) will eventually be needed as to obtain a better characterization of the nonlinear-linear transition if shown to exist.

The sclera also exhibits complex anisotropic characteristics as a result of the multidirectional arrangement of collagen fibers embedded in the proteoglycan-based ground substance matrix [7,15]. Collagen fibers in the sclera have a large distribution of diameters and are formed into irregularly arranged, multilayered lamellae, with each lamella having different principal fiber orientations and thicknesses [8]. Previous studies have found that scleral collagen fibers in the immediate peripapillary region are more organized and oriented predominantly in the circumferential direction relative to the scleral canal [9,10].

Our results suggest a possible correlation between the fiber orientation and the principal directions associated with the maximum principal strain in the region adjacent to the scleral canal (the peripapillary sclera). Other studies have shown that soft tissue structures within the ONH (e.g., neural tissue and lamina cribrosa) are considerably weaker than the surrounding sclera tissue [2,16,17], which would likely cause the maximum principal stress/strain to orient along the tangent to the scleral canal [18,19]. A remodeling theory for living soft tissues has been proposed that postulates that the ultrastructural organization of the collagen fibers is likely to be dictated by the direction and magnitude of the maximum principal strain [20]. According to this theory, it is likely that there would be strong correlation between the collagen fiber orientation and the direction of the maximum principal strain in the peripapillary sclera. In fact, maximum principal strain is oriented circumferentially around the scleral canal, and the collagen fibers are predominantly oriented circumferentially as well [9,10]. Overall, the collagen ultrastructure in the peripapillary sclera could be optimized to withstand IOP-related stress concentrations resulting from the geometry of the scleral canal. This is likely protective of the delicate lamina cribrosa that spans the scleral canal and the axons that pass through the canal at the ONH.

In this study, several limitations warrant further discussion. This technique is limited to the 2D surface strain on planar specimens, and ignores the remaining three components of the 3D finite strain tensor, the radial strain, and the two transverse shearing strains. This limitation is acceptable for a thin-walled isotropic pressure vessel, in which the principal loading axes are tangent to the material surface [21], and can also be acceptable with a moderate confidence for scleral tissue, because the collagen fibers are mostly aligned tangent to the material surface. Therefore, we believe that our 2D optical measurement system composed of a high-resolution digital camera and microscope is sufficiently accurate to extract the principal components of scleral surface strain. It should be noted that the field of view in the 2D optical measurement has to be sufficiently small compared to the diameter of the eye in order to minimize the optical error due to the out-of-focus marker images. The field of view in the current study was chosen to be a  $4 \times 4$  mm in size, and the diameter of each porcine

eye was approximately 25 mm. Using a 2D experimental method to describe the behavior of a 3D soft tissue structure is a first step toward understanding ocular mechanics and its possible implications in glaucomatous damage to the ONH. We are currently developing an optical method to evaluate the full 3D displacement field of monkey posterior sclera under IOP, which will allow us to confirm the presented results.

It is also important to note that the pixel displacement vector obtained from the optical flow algorithm is only an approximation of the actual 2D displacement vector of each marker centroid, and that the predicted pixel displacement vector is likely contaminated by an error (Fig. 3). This is due to the inaccuracy of the Lucas–Kanade approximation as well as to the noise in the marker images. Although this error should be small in each incremental increase of IOP (1 mm Hg), the error could be accumulated to become unacceptably large over multiple incremental steps from 5 mm Hg up to 45 mm Hg. However, our method only used the Lucas–Kanade algorithm to provide a first estimation of marker displacement, so that optical flow errors did not affect the final displacement fields. It should be noted that the optical flow algorithm has been shown to perform well for qualitative purposes but will perform less accurately for quantitative purposes [22].

Finally, the sclera was assumed to be purely elastic, as the process of increasing IOP from 5 mm Hg to 45 mm Hg was repeated four times (one for each quadrant of the eye). As this study was aimed at visualizing surface strains of porcine peripapillary sclera, not at determining scleral stiffness, we concluded that this assumption was a good first approximation. Our new experimental protocol will allow us to measure 3D displacements from the whole posterior scleral shell in a single pressurization cycle.

Mechanical testing and modeling of ocular soft tissues will contribute to our understanding of glaucomatous ONH [2,23,24] and peripapillary scleral [3–5] damage, myopia [8], and a host of other ocular disorders. Since the peripapillary sclera determines the levels of strain and stress placed on the contained ONH, and has been demonstrated to be altered in early experimental glaucoma [4], it is likely to play an important role in glaucomatous damage and warrants further investigation.

## Acknowledgment

This work was supported by the NIH (RO1EY11610, C.F.B.).

## References

- [1] Leske, M. C., 1983, “The Epidemiology of Open Angle Glaucoma: A Review,” *Am. J. Epidemiol.*, **118**(2), pp. 166–191.
- [2] Burgoyne, C. F., Downs, J. C., Bellezza, A. J., Suh, J.-K. F., and Hart, R. T., 2005, “The Optic Nerve Head as a Biomechanical Structure: A New Paradigm for Understanding the Role of IOP-Related Stress and Strain in the Pathophysiology of Glaucomatous Optic Nerve Head Damage,” *Prog. Retin Eye Res.*, **24**, pp. 39–73.
- [3] Downs, J. C., Suh, J.-K. F., Thomas, K. A., Bellezza, A. J., Burgoyne, C. F., and Hart, R. T., 2003, “Viscoelastic Characterization of Peripapillary Sclera: Material Properties by Quadrant in Rabbit and Monkey Eyes,” *ASME J. Biomech. Eng.*, **125**, pp. 124–131.
- [4] Downs, J. C., Suh, J.-K. F., Thomas, K. A., Bellezza, A. J., Hart, R. T., and Burgoyne, C. F., 2005, “Viscoelastic Material Properties of the Peripapillary Sclera in Normal and Early-Glaucoma Monkey Eyes,” *Invest. Ophthalmol. Visual Sci.*, **46**(2), pp. 540–546.
- [5] Girard, M., Suh, J.-K. F., Hart, R. T., Burgoyne, C. F., and Downs, J. C., 2007, “Effects of Storage Time on the Mechanical Properties of Rabbit Peripapillary Sclera After Enucleation,” *Curr. Eye Res.*, **32**(5), pp. 465–470.
- [6] Edelhauser, H. F., and Ubels, J. L., 2003, “The Cornea and the Sclera,” *Adler’s Physiology of the Eye, Clinical Applications*, edited by P. L. Kaufman and A. Alm, 10th ed., Mosby, St. Louis, MO.
- [7] Komai, Y., and Ushiki, T., 1991, “The Three-Dimensional Organization of Collagen Fibrils in the Human Cornea and Sclera,” *Invest. Ophthalmol. Visual Sci.*, **32**(8), pp. 2244–2258.
- [8] Summers Rada, J. A., Shelton, S., and Norton, T. T., 2006, “Review: The Sclera and Myopia,” *Exp. Eye Res.*, **82**, pp. 185–200.
- [9] Kokott, W., 1934, “Das spaltlinienbild der sklera., (Ein beitrag zum funktionellen bau der sklera),” *Klin. Monatsbl. Augenheilkd.*, **92**, pp. 177–185.
- [10] Greene, P. R., 1980, “Mechanical Considerations in Myopia: Relative Effects of Accommodation, Convergence, Intraocular Pressure, and the Extraocular Muscles,” *Am. J. Optom. Physiol. Opt.*, **57**(12), pp. 902–914.

- [11] Barron, J. L., and Klette, R., 2002, "Quantitative Color Optical Flow," *Proceedings of ICPR*.
- [12] Barron, J. L., Fleet, D. J., and Beauchemin, S. S., 1994, "Performance of Optical Flow Techniques," *Int. J. Comput. Vis.*, **12**(1), pp. 43–77.
- [13] Lucas, B. D., and Kanade, T., 1981, "An Iterative Image Registration Technique With an Application to Stereo Vision," *Proceedings of DARPA Image Understanding Workshop*, pp. 121–130.
- [14] Fung, Y. C., 1993, *Biomechanics: Mechanical Properties of Living Tissues*, 2nd ed., Springer-Verlag, New York.
- [15] Watson, P. G., and Young, R. D., 2004, "Scleral Structure, Organization and Disease. A Review," *Exp. Eye Res.*, **78**, pp. 609–623.
- [16] Sigal, I. A., Flanagan, J. G., Tertinegg, I., and Ethier, C. R., 2004, "Finite Element Modeling of Optic Nerve Head Biomechanics," *Invest. Ophthalmol. Visual Sci.*, **45**(12), pp. 4378–4387.
- [17] Spoerl, E., Boehm, A. G., and Pillunat, L. E., 2005, "The Influence of Various Substances on the Biomechanical Behavior of Lamina Cribrosa and Peripapillary Sclera," *Invest. Ophthalmol. Visual Sci.*, **46**(4), pp. 1286–1290.
- [18] Bellezza, A. J., Hart, R. T., and Burgoyne, C. F., 2000, "The Optic Nerve Head as a Biomechanical Structure: Initial Finite Element Modeling," *Invest. Ophthalmol. Visual Sci.*, **41**(10), pp. 2991–3000.
- [19] Sander, E. A., Downs, J. C., Burgoyne, C. F., Hart, R. T., and Burgoyne, C. F., 2006, "A Cellular Solid Model of the Lamina Cribrosa: Mechanical Dependence on Morphology," *ASME J. Biomech. Eng.*, **128**(6), pp. 879–889.
- [20] Driessen, N. J. B., Peters, G. W. M., Huyghe, J. M., Bouten, C. V. C., and Baaijens, F. P. T., 2003, "Remodeling of Continuously Distributed Collagen Fibres in Soft Connective Tissues," *J. Biomech.*, **36**, pp. 1151–1158.
- [21] Timoshenko, S., 1970, *Theory of Elasticity*, 3rd ed., McGraw-Hill, New York.
- [22] Verri, A., and Poggio, T., 1987, "Against Quantitative Optical Flow," *Proceedings of the First International Conference on Computer Vision*, pp. 171–180.
- [23] Bellezza, A. J., Rintalan, C. J., Thompson, H. W., Downs, J. C., Hart, R. T., and Burgoyne, C. F., 2003, "Deformation of the Lamina Cribrosa and Anterior Scleral Canal Wall in Early Experimental Glaucoma," *Invest. Ophthalmol. Visual Sci.*, **44**(2), pp. 623–637.
- [24] Burgoyne, C. F., Downs, J. C., Bellezza, A. J., and Hart, R. T., 2004, "Three-Dimensional Reconstruction of Normal and Early Glaucoma Optic Nerve Head Connective Tissues," *Invest. Ophthalmol. Visual Sci.*, **45**(12), pp. 4388–4399.